

Article

Effect of Boron on Microstructures and Low-Temperature Impact Toughness of Medium-Carbon CrMo Alloy Steels with Different Quenching Temperatures

Qiang Wang ^{1,2}, Qian Wang ^{1,2,*}, Qingfeng Wang ³, Chongchong Li ² and Kefu Li ²

¹ School of Materials Engineering, North China Institute of Aerospace Engineering, No.133 Aimindong Road, Langfang 065000, China; 18783477816@163.com

² Hebei Provincial Key Laboratory of Thermal Protection Materials, North China Institute of Aerospace Engineering, No.133 Aimindong Road, Langfang 065000, China; hgdlichong@163.com (C.L.); shendaozhan@163.com (K.L.)

³ Laboratory of Metastable Materials Science and Technology, Yanshan University, Qinhuangdao 066004, China; wqf67@ysu.edu.cn

* Correspondence: wqhh0316@163.com

Abstract: The effect of boron (B) on the microstructures and low-temperature impact toughness of medium-carbon CrMo steel quenched at 870~1050 °C and tempered at 600 °C was studied via Charpy impact testing and microstructure characterizations. The results showed that with an increasing B content from 0 to 50 ppm, the low-temperature impact toughness deteriorated significantly at quenching temperatures (T_q) lower than 950 °C but increased at a higher T_q of 1050 °C. Undissolved M_2B particles remained and coarsened during the holding process due to the low T_q , decreasing the critical stress required for crack initiation and deteriorating the impact toughness accordingly. However, this detrimental effect of B could be mitigated by a higher T_q , and the favorable influences on the impact toughness improvement could be attributed to (1) the finer M_2B particles formed during quenching effectively pinning the austenite grain boundaries (GBs), leading to a finer block size and a high density of high-angle grain boundaries, which reduced the critical stress for crack initiation; and (2) the fact that the coarsening of $M_{23}C_6$ on the GBs during tempering was slightly suppressed by the segregated B, eventually increasing the energy required for crack propagation. However, the degree of the favorable effect due to B was still lower than the negative effect of a high T_q .

Keywords: boron; M_2B ; $M_{23}C_6$; density of high-angle grain boundaries; low-temperature impact toughness



Citation: Wang, Q.; Wang, Q.; Wang, Q.; Li, C.; Li, K. Effect of Boron on Microstructures and Low-Temperature Impact Toughness of Medium-Carbon CrMo Alloy Steels with Different Quenching Temperatures. *Processes* **2024**, *12*, 852. <https://doi.org/10.3390/pr12050852>

Academic Editor: Chin-Hyung Lee

Received: 26 March 2024

Revised: 16 April 2024

Accepted: 20 April 2024

Published: 23 April 2024



Copyright: © 2024 by the authors. Licensee MDPI, Basel, Switzerland. This article is an open access article distributed under the terms and conditions of the Creative Commons Attribution (CC BY) license (<https://creativecommons.org/licenses/by/4.0/>).

1. Introduction

As a common commercial steel, medium-carbon CrMo steel has been widely used for structures and the production of machine parts, for example, oil well tubing, drill pipes, train axles, and high-strength bolts [1–3]. The type of tempered sorbite that possesses favorable comprehensive mechanical properties is generally expected through the heat treatment of quenching and high-temperature tempering. Additionally, boron (B) of a ppm scale is primarily used to improve the hardenability of medium-carbon CrMo steels, particularly in thick plate production. It is widely understood that B, as a surface-active element, can easily segregate on austenite grain boundaries (GBs), lowering the GB energy and thereby inhibiting the nucleation of ferrite or bainite [4–6]. Meanwhile, the B atoms segregated on the GBs are known to be beneficial for improving the mechanical properties, and the probable mechanisms are summarized as follows: (1) B atoms can enhance the GB cohesion energy by filling vacancies or forming covalent bonds; (2) the stress concentrations at the GBs can be relieved by facilitating GB dislocation movements [7–9]; (3) B can decrease the intergranular segregation of phosphorus at the GBs through a competitive mechanism and reduce the occurrence of cold brittleness [7,10,11]; and (4) the addition of B may stabilize

austenite and contribute to the formation of fine grains, thereby simultaneously improving the strength and toughness [12,13]. However, it is worth noting that all of the above favorable effects are based on the fact that B can effectively segregate on GBs. Depending on the thermal cycle, B can segregate on GBs through equilibrium segregation (ES) or non-equilibrium segregation (NES) mechanisms [14]. On the one hand, the ES results from the system total energy reduction caused by the migration of the solute B atoms from the matrix to GBs. For an identical solute concentration in steel with a certain composition, the ES magnitude decreases with an increasing temperature. On the other hand, the NES has been derived on the basis of the vacancy-dragging mechanism. The NES magnitude increases with an increasing quenching temperature and a decreasing cooling velocity [14–16].

However, as affected by the thermal cycle and B content, B may also be incorporated into boron precipitates, whose morphology and distribution will have a significant influence on the mechanical properties of the steel, for example, the yield strength and impact toughness. Previous investigations have shown that the best balance of strength and toughness is generally obtained with a B content in the range of roughly 10 to 40 ppm [7,17,18]. For example, Taylor et al. [10] investigated the boron precipitation in 0.2 wt.%C-10 ppmB carbon steel and demonstrated that iron borocarbide particles precipitated along the austenite GBs during cooling from 1260 °C to 870 °C. The coarsening of such precipitations might occur with an increasing B content and by prolonging the holding time, which finally lowers the Charpy upper-shelf energy. A similar phenomenon was found by Zheng et al. [4], where iron borocarbide particles were analyzed in detail and identified as M_2B . The authors suggested that although the M_2B particles were refined with the increasing austenitizing temperature, the distribution of these particles, which were mainly concentrated on the GBs due to the excessive B segregation, reduced the impact toughness significantly. Cao et al. [17] reported that an increased B content strengthened the co-segregation behavior and promoted the precipitation of B-containing oxides, which were mainly distributed on the original austenite GBs and deteriorated the low-temperature impact toughness of the weathering steel weld metal. Additionally, for steels that require tempering treatment or suffer from long-term service in high-temperature environments, an increase in the B content led to the formation of chains of closely spaced $M_{23}C_6$ carbides at the lath boundaries. The formation of numerous voids, which were found at the carbide–matrix boundaries, resulted in the appearance of cracks with critical dimensions and decreased the impact toughness of the 10% Cr steel [18]. Hong et al. [7] also found that when plain carbon steels were added with an amount of B higher than 20 ppm or isothermally treated at 550 °C~650 °C for over 3 h, intergranular fracturing would occur. Due to the lack of detailed characterization of the boundary precipitates, for the related mechanism, it was speculated that the particles of $M_{23}(C,B)_6$ or $M_3(C,B)$ precipitated by consuming B atoms segregated on the GBs, which acted as intergranular crack initiation sites and decreased the toughness. However, in some studies, B was found to be incorporated into $M_{23}C_6$ carbides at the GBs, suppressing the agglomeration of $M_{23}C_6$ carbides with a continuous film shape, which act as potential sites of microcrack nucleation and propagation and deteriorate the mechanical properties [19,20]. Tabuchi et al. [21] further reported that the high B content provided for two-phase separation of $M_{23}C_6$ carbides into B-free $M_{23}C_6$ carbides and $M_{23}(BC)_6$ phase, which led to the refinement of these particles to 70 nm and improved the impact toughness of a boron-doped 9Cr-steel.

To date, although considerable research has been carried out on the relationship between B addition and impact toughness, it is not easy to make good use of B in industrial production processes as its state under different kinds of heat treatments and a varied B content is still unclear and requires further research. In addition, previous studies have mainly focused on low-carbon steel or high-Cr heat-resistant steel, and there are few studies on the effect of B on the performance of medium-carbon CrMo steel. For example, Gárlipp et al. [13] studied the effect of different continuous cooling rates on the microstructure transformation of 0.2C-1.14Mn-0.0030B steel. However, the evolution of B-containing precipitations under different cooling rates and their effects on the mechanical properties were not investigated. Similar research was undertaken by Taylor et al. [10],

but the relationship between the segregation and precipitation of boron and the impact toughness was discussed in detail for 0.2C-0.6Mn-0.5Mo-B steels after holding at 870 °C for various amounts of time, followed by quenching and tempering. Furthermore, Bai et al. [5] investigated the effect of the B distribution and its existence state on quench cracking for a medium-carbon microalloyed steel quenched at 880 °C with water. They found that the segregation of B on the austenite GBs enhanced the impact toughness, but the ductility of the steel deteriorated significantly when B was densely distributed on the GBs as a brittle precipitated phase. Zheng et al. [4] further studied the state of the B in the different quenching processes and their relationships with the toughness of 25CrMoNbB steel. Although, as the dissolved temperature of B-containing precipitation such as Fe₂B is generally high, it is far from satisfactory to discuss the dissolution and precipitation behaviors at temperatures lower than 1000 °C. Additionally, it should be noted that martensitic substructures might also affect the impact toughness by controlling crack propagation [22–26]. For example, Zhou et al. [22,23] indicated that both packet and block boundaries could inhibit crack propagation by acting as barriers. Zhang et al. [24] reached a similar conclusion and further suggested that blocks with high-angle grain boundaries (HAGBs) are the minimum control structural units for 25CrMo48V steel. Yang et al. [25] claimed that the increase in the crack propagation path was attributed to the refinement of the block and the increased HAGBs. Kang et al. [26] suggested that the ferrite–martensite interfaces with high-angle misorientation contributed to the improved impact toughness of the high-strength low-alloy steel by analyzing the second crack propagation with SEM and EBSD. Thus, the microstructural differences caused by B and their effects on the impact toughness should also be fully addressed from the perspective of crystallography and morphology when discussing the influence of B on the impact toughness under different heat treatment processes. However, unfortunately, both of the two points just mentioned are not fully considered in the previous research.

In the present study, the microstructures and low-temperature impact toughness of medium-carbon CrMo steels with varying levels of B after different quenching and tempering treatments were researched to explore the function of B. This better understanding of the influences of B on the microstructures and impact toughness will help establish methods to expand the application of B-containing medium-carbon low-alloy steels.

2. Materials and Methods

Medium-carbon low-alloy steels with a target B content of 0 ppm, 15 ppm, and 50 ppm were chosen for this study. They were melted by using a 50 kg vacuum furnace and hot-rolled to plates of 12 mm thickness. The chemical compositions of the steel plates with a B content of 0 ppm, 15 ppm, and 50 ppm are shown in Table 1, labeled 0B, 15B, and 50B, respectively. It is worth mentioning that the selected steel was categorized as “medium-carbon” steel based on its carbon equivalent C_{eq} , considering the presence of C, Cr and Mo. The C_{eq} was calculated by Equation (1) as 0.548 wt.%, which falls within the range of 0.3–0.6 wt.% [27]. Titanium was added to stabilize the nitrogen (N) as TiN in order to reduce the consumption of B due to the reaction between N and B.

$$C_{eq} = C + Mn/6 + (Cr + V + Mo)/5 + (Cu + Ni)/15 \quad (1)$$

Table 1. Chemical compositions of the test steels in wt.%.

Steel	C	Mn	Si	Cr	Mo	Ti	B	N
0B	0.26	0.51	0.26	0.87	0.57	0.012	0	≤0.003
15B	0.26	0.50	0.26	0.87	0.55	0.012	0.0015	≤0.003
50B	0.26	0.48	0.25	0.86	0.56	0.012	0.0050	≤0.003

The specimens were 150 × 60 × 12 mm³ in size, as cut from the steel plates. Then, the hot-rolled specimens 0B, 15B, and 50B were quenched from 870 °C, 950 °C, and 1050 °C for

15 min, respectively, followed by water-cooling to room temperature. The quenched specimens were then tempered at 600 °C for 60 min, followed by air-cooling to room temperature.

The quenched samples obtained were mechanically polished and chemically etched with picric acid to observe the morphology and distribution of the austenitic phase. Samples that were heat-treated using the quenching and tempering (QT) process were etched in 4% nital, and the morphology of the microstructure was preliminarily observed by using a metallographic microscope (axiover-200mat) (ZEISS, Jena, Germany) and further characterized with an S3400 scanning electron microscope (SEM) (Hitachi, Tokyo, Japan). The specimens for electron back-scattered diffraction (EBSD) were first mechanically polished, then precise-polished using a 0.04 µm suspension of colloidal silica particles. The EBSD maps were obtained by using a SUPRA550 field emission microscope (Hitachi, Tokyo, Japan). The martensitic packet and block and the distribution of the misorientation angles between the GBs were revealed by a TSL orientation imaging microscopy system. The characteristics of the martensitic lath and precipitates were characterized by examining thin foils and carbon extraction replicas using a JEM-2010 high-resolution transmission electron microscope (HR-TEM) (JEOL, Tokyo, Japan). Then, the average equivalent diameter d_p and volume fraction f of the precipitated particles in each specimen were estimated from the TEM images. However, since the morphology of the precipitates in the as-tempered samples varied, it was hard to make a direct comparison based on their actual measured dimensions. Therefore, the precipitates with different shapes were considered spherical for better comparison. The area of each precipitated particle measured directly using Image-Pro software was regarded as the projection circle area of the equivalent spherical shape of the precipitate. The equivalent diameter of a single particle was then calculated according to Equation (2). The average equivalent diameter was statistically obtained by measuring at least 100 particles for each specimen. The volume fraction of the particles f was calculated using Equation (3).

$$S = \pi d_p^2 / 4 \quad (2)$$

$$f = \frac{N \frac{4\pi}{3} \left(\frac{d_p}{2}\right)^3}{S_0 d_p} = \frac{N \pi d_p^2}{6 S_0} = \frac{2 N S}{3 S_0} \quad (3)$$

where, N is the number of particles per area, S_0 is the specific area for estimation, and S is the particle area measured directly with Image-Pro software (Version 6.0).

To conduct the Charpy impact tests, the QT-treated samples were machined into normative Charpy V-notch samples of 10 × 10 × 55 mm³. The Charpy impact tests were performed at temperatures ranging from −80 °C to −20 °C. Impact testing for each temperature was performed on at least three separate specimens in accordance with the Standard of ASTM E23 [28]. An SEM was used to observe the fracture surfaces of the specimens, and the second crack propagation was characterized from the section perpendicular to the notch using an SEM and EBSD.

3. Results

3.1. Charpy Impact Toughness

The average Charpy absorbed energy tested at −80 °C, −60 °C, and −20 °C for the different QT-treated specimens with varying B content is shown in Figure 1. As expected, the Charpy absorbed energy values all decreased with a decreasing test temperature, and with the B content increasing from 0 to 50 ppm, the low-temperature impact toughness deteriorated significantly at quenching temperatures (T_q) lower than 950 °C but increased at a higher T_q of 1050 °C. Considering the consistency change rule at different test temperatures, the impact toughness of the samples tested at −60 °C against the B content and quenching temperature (T_q) was taken as an example, and the impact values are described in detail in this section. This finding shows that when the steels in this experiment were quenched at a relatively low T_q , e.g., 870 °C and 950 °C, the average Charpy absorbed energy decreased significantly from 160 J to 32 J and from 156 J to 23 J, respectively, with the B content increasing from 0 to 50 ppm. However, when the steel specimens were quenched

at a higher T_q of 1050 °C, the average Charpy absorbed energy increased from 9 J to 69 J, which implies the different state of B under a varying T_q and its changing effect on the impact toughness. In addition, three possible reasons may account for the high impact value at negative temperatures for the steel: (1) generally, the longitudinal impact is higher than the transverse impact and the Charpy samples in this experiment were cut parallel to the rolling direction of the steel plate; (2) the metallurgical quality of the steel is high; and (3) a tempered sorbite structure was obtained with high-temperature tempering.

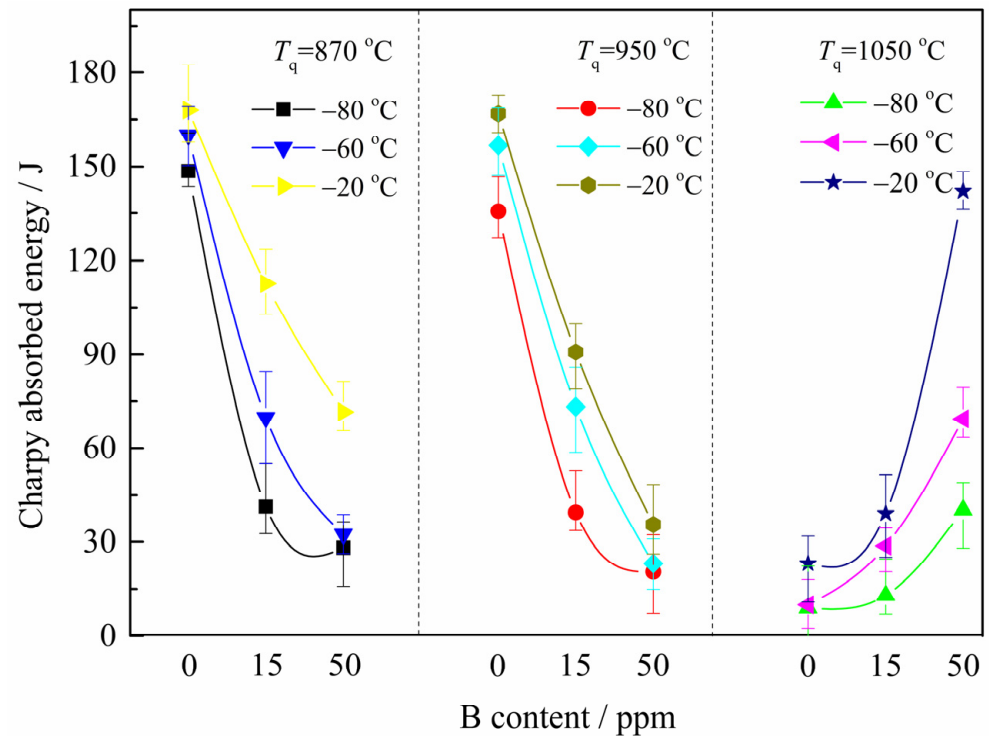


Figure 1. Average Charpy absorbed energy tested at -80 °C , -60 °C , and -20 °C for different QT-treated specimens with varying B content.

3.2. Microstructure Observation

Since the average Charpy absorption energy of the samples tested at -60 °C changes monotonically with the B content under different T_q , the samples that had a B content of 0 and 50 ppm and that were each quenched at 870 °C and 1050 °C were selected for microstructure and fracture surface analysis. The above samples were marked as 0B-870, 50B-870, 0B-1050, and 50B-1050, respectively, for readability.

3.2.1. Prior Austenite Grain (PAG) Observation

The typical morphology and the average grain size of the PAG in the as-quenched 0B-870, 50B-870, 0B-1050, and 50B-1050 specimens are shown in Figure 2 and Table 2, respectively. For an identical T_q of 870 °C, there was no significant difference in the macromorphology and average grain size of the PAG (D_γ) between the 0B-870 and 50B-870 specimens. Meanwhile, the shape of the PAG was almost equiaxed, and the average grain size of the PAG was about 38 μm . Moreover, as the T_q increased from 870 °C to 1050 °C, the austenite grains coarsened remarkably. However, compared to the specimen with 50 ppm B, the average grain size of the PAG of the 0B-1050 specimen was larger and some abnormal-growth grains were revealed due to extreme superheating, which suggests that B may inhibit the grain growth somewhat.

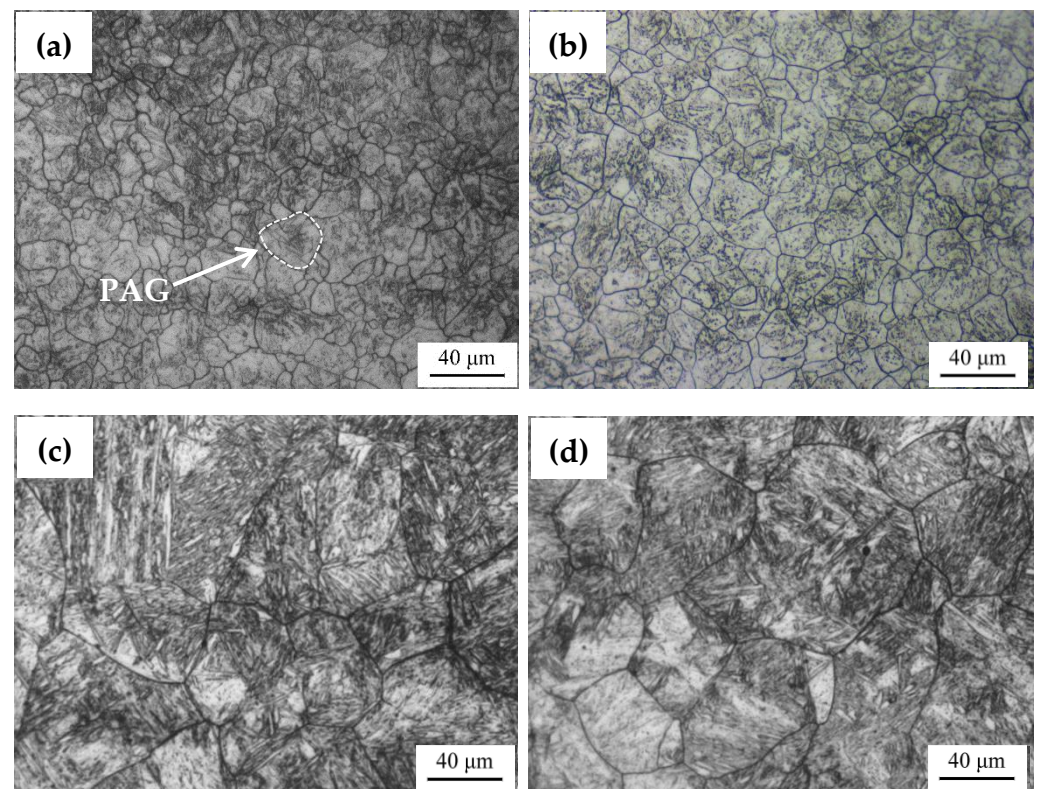


Figure 2. Typical observations of the PAG in the as-quenched (a) 0B-870, (b) 50B-870, (c) 0B-1050, and (d) 50B-1050 specimens.

Table 2. Summary of the microstructure observations and quantifications.

Samples	$D_r/\mu\text{m}$	$D_p/\mu\text{m}$	$D_b/\mu\text{m}$	$D_{\text{GBMA} \geq 15^\circ}/\mu\text{m}^{-1}$	d_{pi}/nm	$f_i/\%$	d_{pg}/nm	$f_g/\%$
0B-870	38.7 ± 3	5.2 ± 0.2	1.4 ± 0.08	1.16 ± 0.02	43 ± 8	0.12 ± 0.04	111 ± 4	0.32 ± 0.02
50B-870	37.3 ± 3	5.1 ± 0.2	1.5 ± 0.07	1.18 ± 0.03	48 ± 4	0.10 ± 0.04	159 ± 5	0.52 ± 0.02
0B-1050	75.7 ± 4	12.7 ± 0.2	2.4 ± 0.07	0.87 ± 0.02	54 ± 3	0.15 ± 0.05	102 ± 3	0.60 ± 0.03
50B-1050	66.1 ± 2	9.4 ± 0.3	2.1 ± 0.06	0.97 ± 0.02	47 ± 8	0.16 ± 0.02	73 ± 4	0.65 ± 0.02

D_r —average grain size of the PAG; D_p —mean size of the packet; D_b —mean size of the block; $D_{\text{GBMA} \geq 15^\circ}$ —the density of the high-angle grain boundaries; d_{pi} —mean equivalent diameter of the precipitates in the matrix grain; f_i —volume fraction of the precipitates in the matrix grain; d_{pg} —mean equivalent diameter of the precipitates on the GBs; f_g —volume fraction of the precipitates on the GBs.

3.2.2. Packet and Block Observation

It is well known [29] that the lath morphology may be regarded as a hierarchic structure of the parent PAG–packet–block–individual lath, one of which may act as the minimal microstructural unit controlling crack propagation. Thus, the typical morphology of the martensite packet and block in the as-tempered 0B-870, 50B-870, 0B-1050, and 50B-1050 specimens was observed by SEM and EBSD, as shown in Figures 3 and 4, respectively. Their average grain sizes were also evaluated, as displayed in Table 2, which shows that the evolution tendency of the mean size of the PAG (D_p) and the mean size of the block (D_b) against an increasing T_q and B content was essentially consistent with the D_γ . It is noteworthy that some discontinuous chains of particles with an average size of around 420 nm, which were mainly distributed on the GBs, were detected in the 50B-870 specimen (marked with red arrows in Figure 3d), whereas these particles were not found in the other specimens.

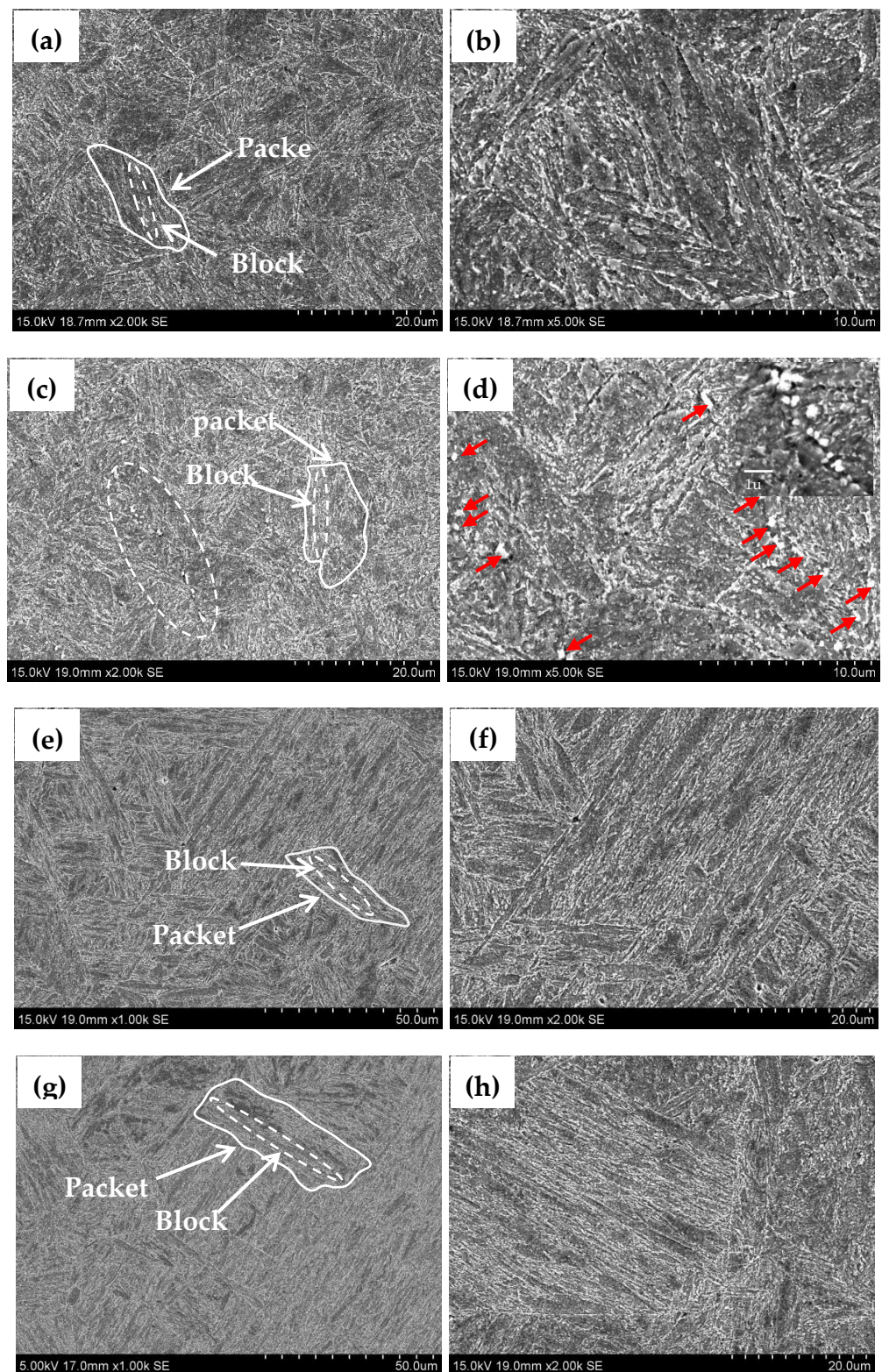


Figure 3. Typical SEM observations of the martensitic packet in the as-tempered (a,b) 0B-870, (c,d) 50B-870, (e,f) 0B-1050, and (g,h) 50B-1050 specimens with different magnifications.

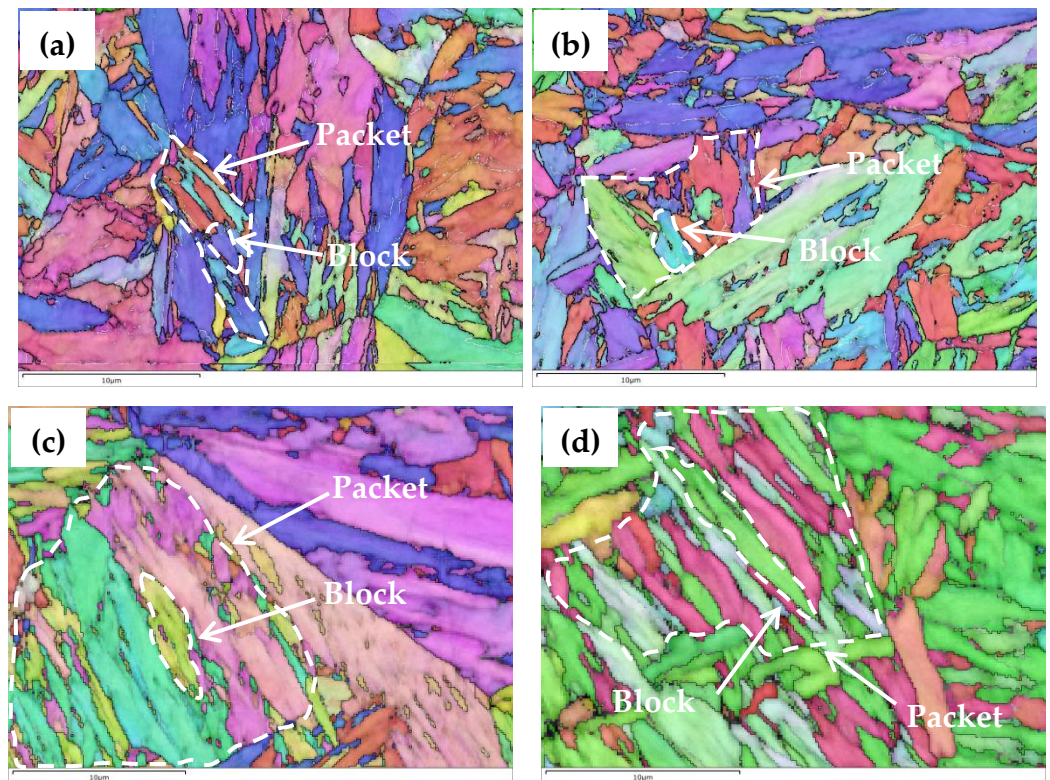


Figure 4. Typical EBSD inverse pole figure map of the martensite block in the as-tempered (a) 0B-870, (b) 50B-870, (c) 0B-1050, and (d) 50B-1050 specimens.

The grain boundary misorientation angle (GBMA) may play a significant role in controlling the impact crack propagation [30]. Therefore, the GBMA distributions of the microstructure were also analyzed by EBSD and the density of the HAGBs, which were defined as GBs with misorientation angles higher than 15° , $D_{GBMA \geq 15^\circ}$, for each specimen was quantified from the kernel average misorientation maps, as shown in Figure 5 and as summarized in Table 2. As this table shows, the $D_{GBMA \geq 15^\circ}$ changed slightly from $1.16 \mu\text{m}^{-1}$ to $1.18 \mu\text{m}^{-1}$ with an increasing B content under the T_q of 870°C but increased obviously from $0.87 \mu\text{m}^{-1}$ to $0.97 \mu\text{m}^{-1}$ under the T_q of 1050°C . Additionally, as the temperature increased, the overall $D_{GBMA \geq 15^\circ}$ showed a decreasing trend.

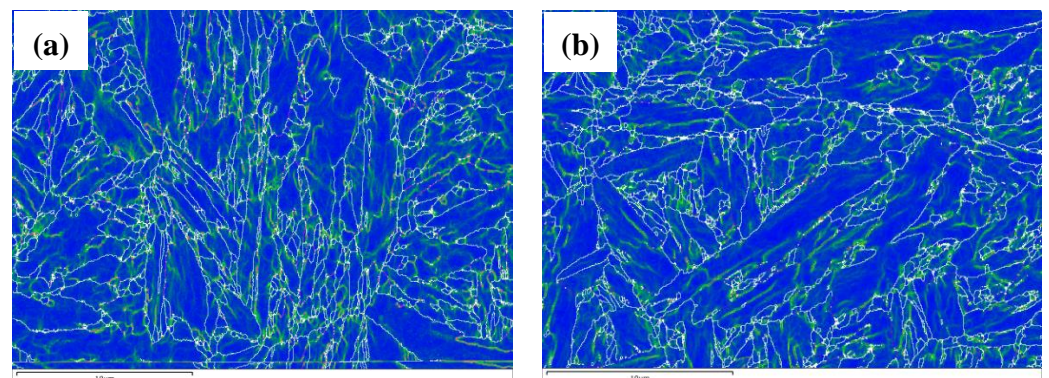


Figure 5. Cont.

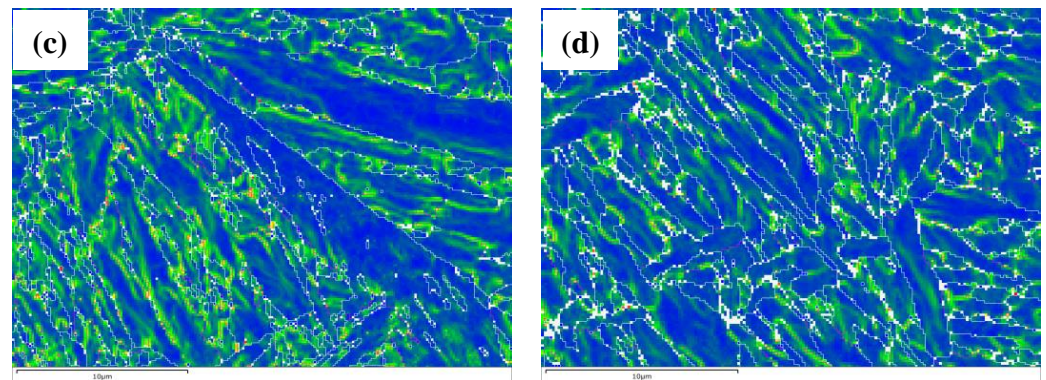


Figure 5. Typical EBSD kernel average misorientation (KAM) maps of the martensite block in the as-tempered (a) 0B-870, (b) 50B-870, (c) 0B-1050, and (d) 50B-1050 specimens.

3.2.3. Observation of Precipitates

(1) Precipitates in matrix grains

Microstructural investigations were carried out in more detail on the as-tempered 0B-870, 50B-870, 0B-1050, and 50B-1050 specimens by using TEM. Figure 6a–d show a bright field image, the corresponding selected area electron diffraction (SAED) patterns, and the energy dispersive spectroscopy (EDS) results of the 0B-870 specimen. The figure shows that numerous short rod-like precipitates were uniformly distributed in the matrix grains, as marked by the white arrows. These precipitates, which are commonly found in TEM analysis of CrMo steel after QT heat treatment, were identified as M_3C through the Miller Index of the SAED pattern in Figure 6b. M_3C was considered to be transformed from ϵ -carbides, which were often found in the same martensite lath/plate at an angle of about 60° to the phase boundary and formed in the self-tempering process based on previous research [31]. The average equivalent size d_{pi} and volume fraction f_i of the precipitated particles in the matrix grains of each steel specimen were estimated. They are shown in Table 2, which indicates that with the T_q increasing to 1050 °C for 0B steel, the size changed little but the volume fraction of the precipitates in the matrix grains slightly increased. According to the thorough study by Morito and Hutchinson [32], the relationship between the dislocation density (ρ) and carbon concentration (wt.%) in martensite can be expressed by the following equation:

$$\rho \times 10^{-15} = 0.7 + 3.5 \times wt.\% C \quad (4)$$

As the T_q increased, the dissolution of carbides formed in the rolling process increased, leading to the increased carbon concentration and corresponding dislocation density in martensite based on the above equation, which promoted precipitation by providing preferential nucleation sites and accordingly increased the number and volume fraction of the precipitates during the tempering process [33]. Additionally, dislocations are known to provide a fast diffusion channel for atoms, which could accelerate the process of precipitation coarsening [34]. On the other hand, dislocations could also facilitate a decrease in precipitate size due to a smaller inter-particle spacing [35]. The above synthetic effects resulted in the constant sizes of the precipitates in the grain matrix, even at higher temperatures. Figure 6g,i provide TEM images of the as-tempered 50B-870 and 50B-1050 specimens. It can be seen that there is no significant difference in the morphology of the precipitates in the matrix grains compared with the 0B samples. The d_{pi} and f_i shown in Table 2 indicate that the differences in the d_{pi} and f_i of the precipitates in the matrix grains were small between the 0B and 50B steel.

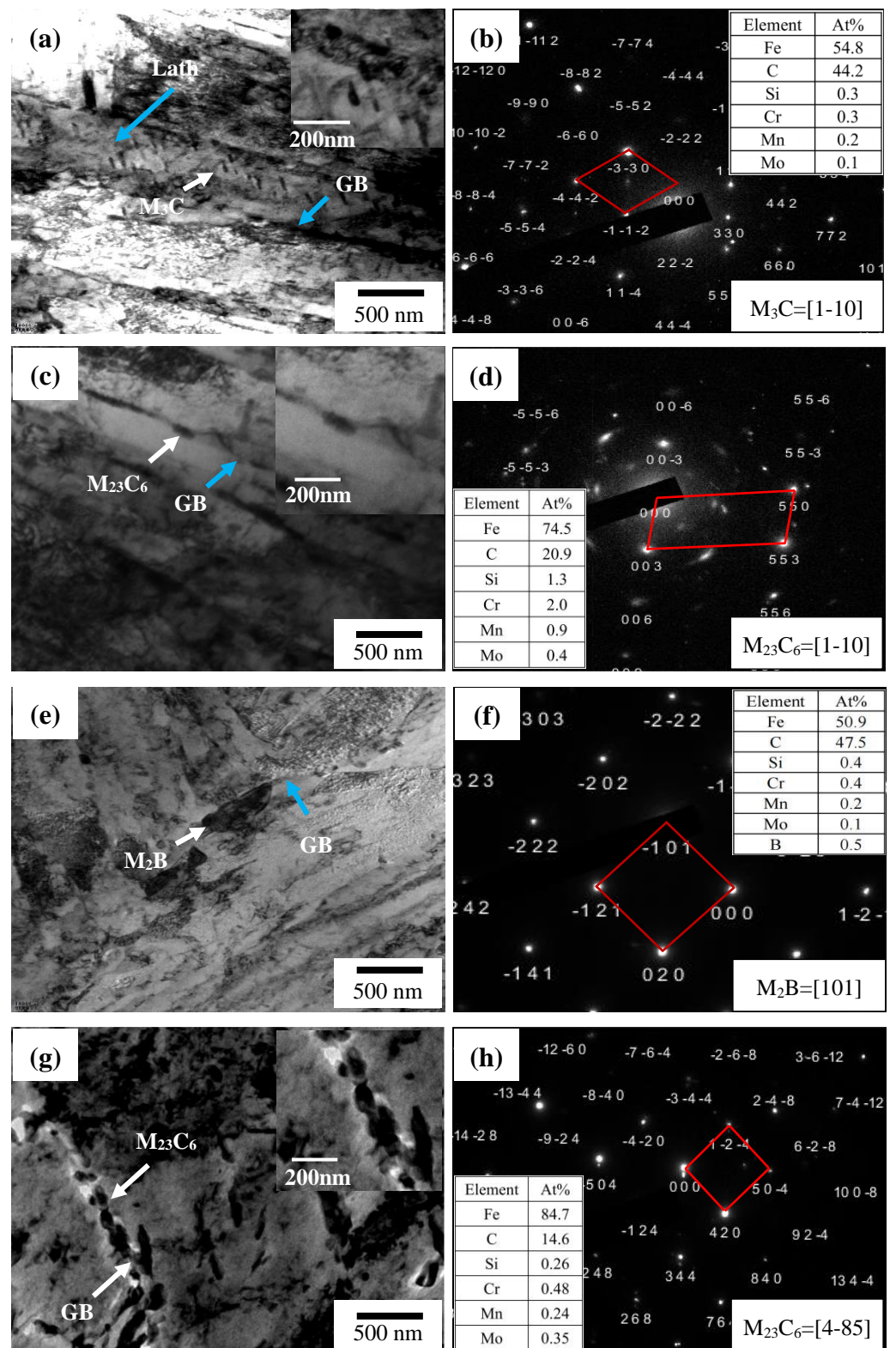


Figure 6. Cont.

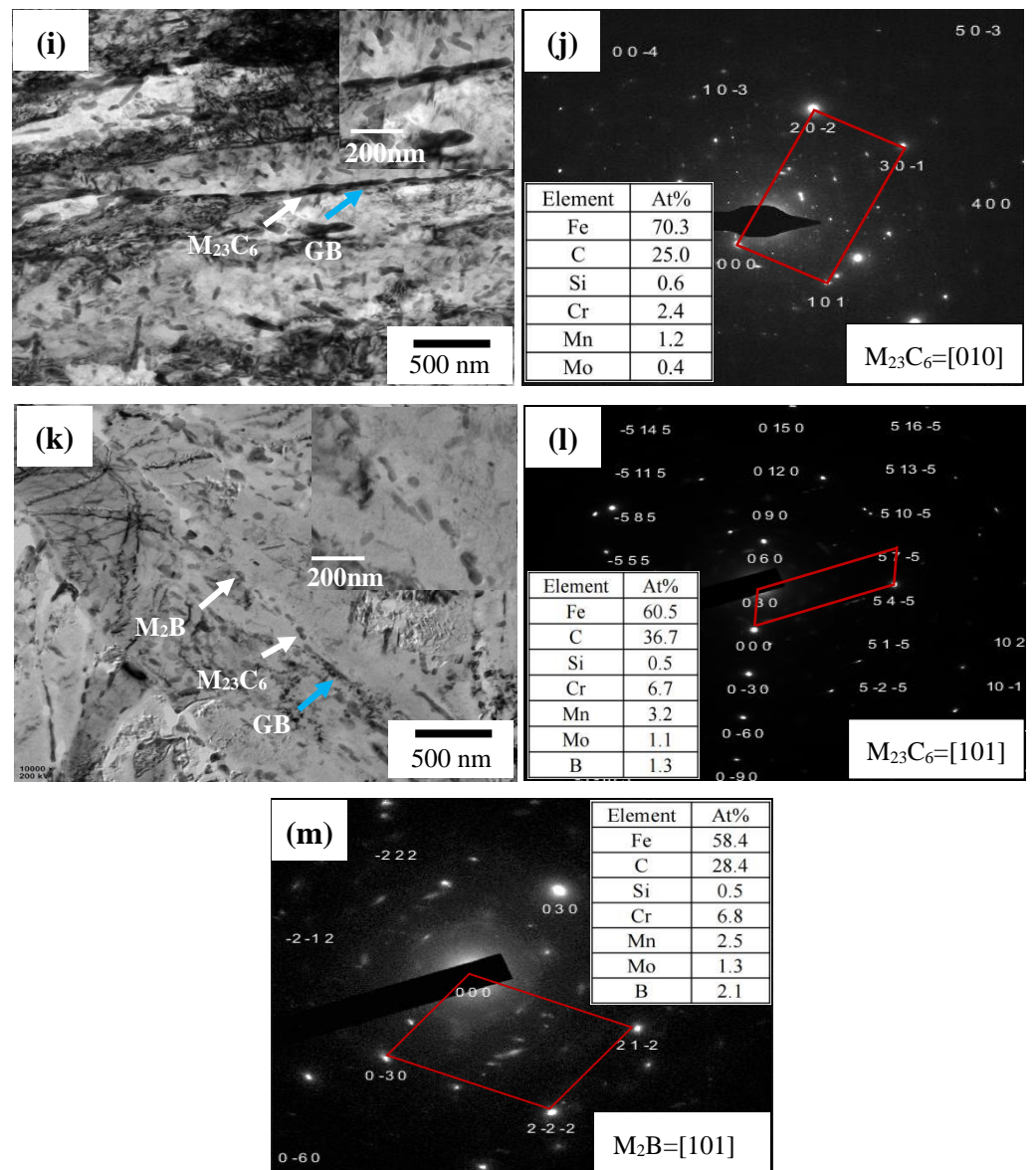


Figure 6. Typical TEM observations of the microstructure and the selected area diffraction pattern and EDS of the corresponding precipitate in samples of (a–d) 0B-870, (e–h) 50B-870, (i,j) 0B-1050, and (k–m) 50B-1050.

(2) Precipitates in GBs

It has frequently been reported that $M_{23}C_6$ carbides with a continuous film shape that occupy the GBs may act as potential sites of microcrack nucleation or propagation and deteriorate the mechanical properties [19,30]. The TEM morphologies of the precipitates on the GBs in each steel are shown in Figure 6. Some continuous blocky carbides around 150 nm are observed on the GBs in the 0B-870 and 50B-870 specimens and are identified as $M_{23}C_6$, as shown in Figure 6c,d,g,h. Additionally, the coarse particles around 420 nm on the GBs that were identified as M_2B are only observed in the 50B-870 specimen, as shown in Figure 6e,f. Moreover, for the 0B specimen, the higher T_q of 1050 °C resulted in denser vermicular-shaped particles distributing on the GBs. However, for the 50B-1050 steel, the coarse M_2B on the GBs in the 50B-870 specimen disappeared and was replaced by the small-size M_2B (around 70 nm), which is shown in Figure 6k,m. As coarse particles located at various GBs are detrimental to the impact toughness, the d_{pg} and their corresponding f_g on various GBs in each specimen were evaluated and are shown in Table 2. It can be seen that the f_g of the carbides on the GBs increased with the quenching temperature for the

steels with identical B content. Interestingly, the d_{pg} increased with the B content increasing from 0 to 50 ppm under the T_q of 870 °C but decreased under the T_q of 1050 °C. Moreover, as indicated in Figure 6l, B was found incorporated into the carbide on the GBs, which was identified as $M_{23}C_6$, implying that the $M_{23}C_6$ might be refined by B addition.

3.2.4. Fracture Surface Observation

The impact fracture surfaces of the 0B-870, 50B-870, 0B-1050, and 50B-1050 specimens tested at -60 °C were observed using an SEM and are shown in Figure 7. The fracture surface for each specimen can be divided into three parts: (1) the fibrous zone of stable crack propagation, (2) the unstable crack propagation zone, and (3) the shear-lip zone of arrested crack propagation. High-magnification views of these three parts for each specimen correspond to Figure 7(a–3a,b–3b,c–3c,d–3d). Figure 7a shows that the ductile dimpled fractures dominated the fracture regions for the impact fracture surface of the 0B-870 specimen. Figure 7(2b,3b) show the impact fracture surface of the 50B-870 specimen; the dimples were replaced by much more significant river patterns or tongues, dividing the fracture surface into several large areas, which were much smoother and flatter, with little roughness. Moreover, the unstable crack propagation zone occupied most of the fracture surface, as indicated in Figure 7b. Moreover, it can be seen from a comparison of Figure 6a,c that the unstable crack propagation zone expanded and the fibrous zone shrank with the T_q increasing from 870 °C to 1050 °C for the steel without B. The impact fracture surfaces of the steel with 50 ppm B addition under an identical T_q of 1050 °C are shown in Figure 6d. It illustrates that the brittle fracture zones were dominated by high-density river-like patterns and tear ridges with small dimples. However, the sizes of the cleavage facets were smaller and the ductile fracture bands between the junctions of the cleavage facets that were considered as the main energy-absorbing mechanism in the crack propagation process were wider, compared with those of 0B-1050 [36].

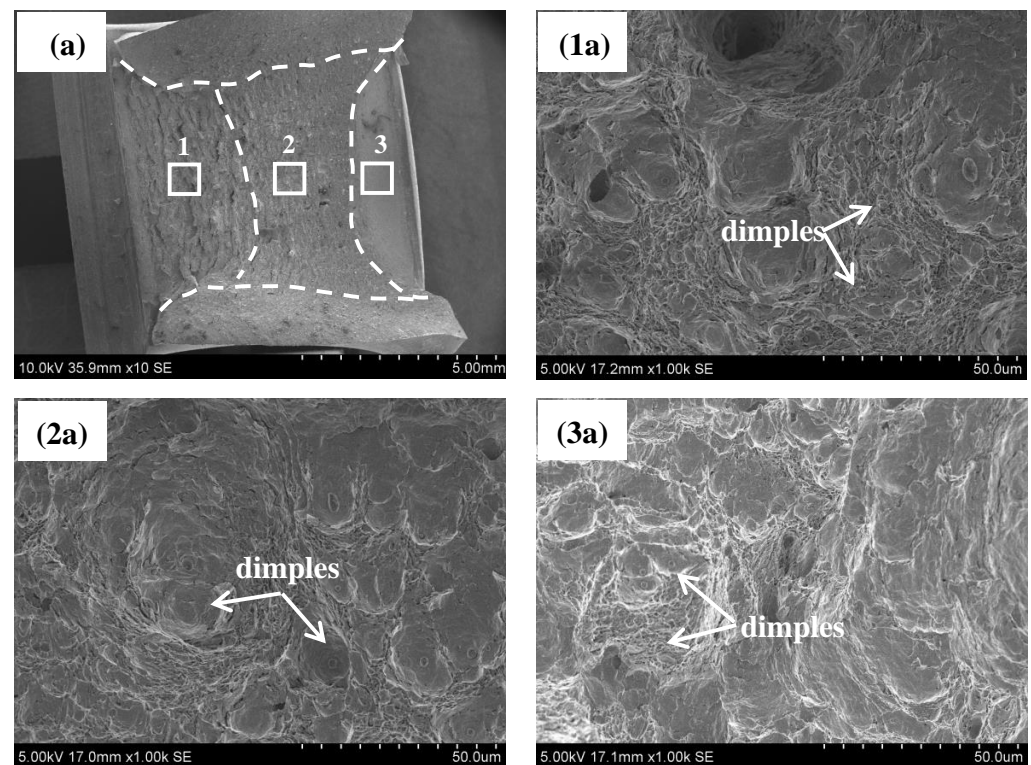


Figure 7. Cont.

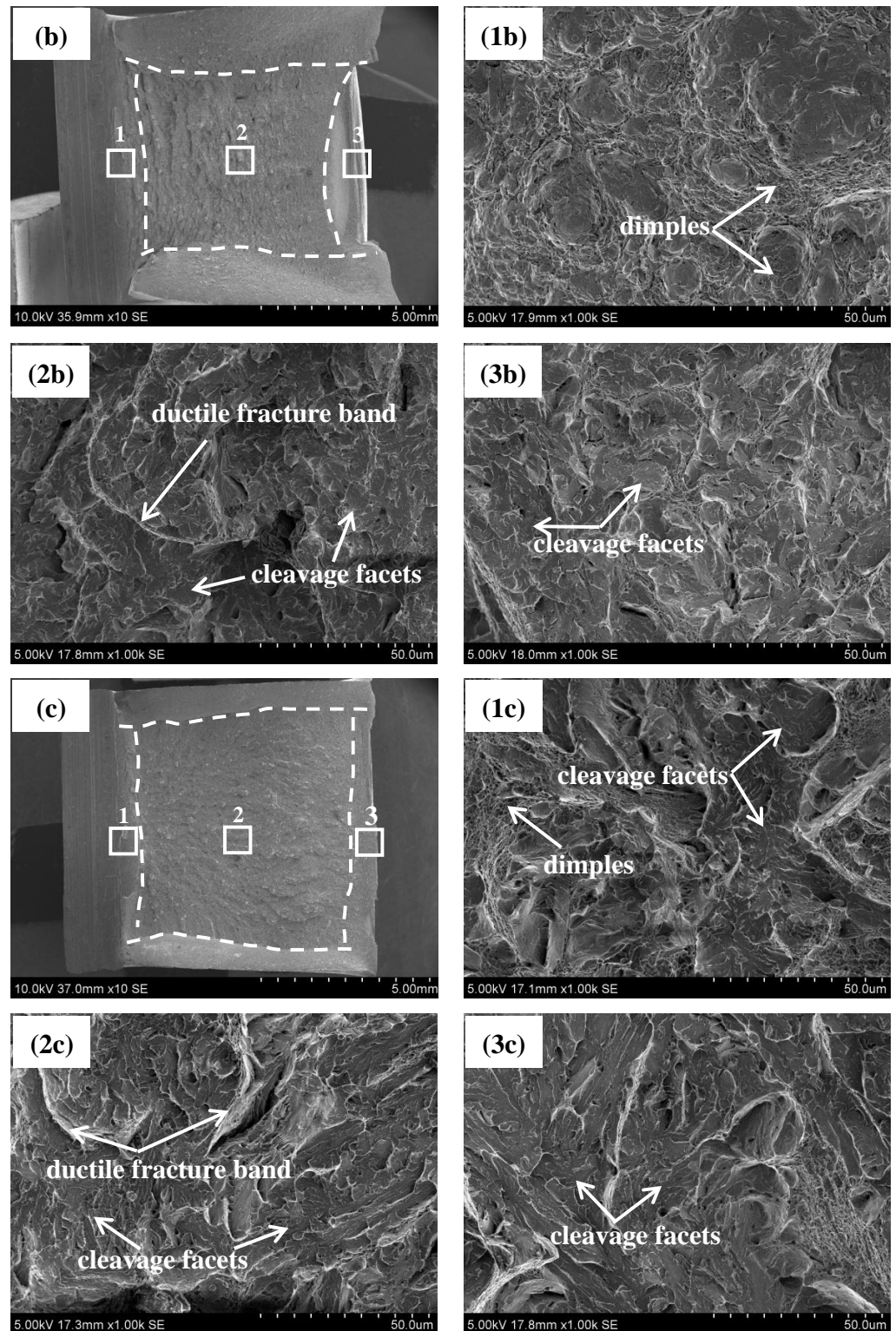


Figure 7. Cont.

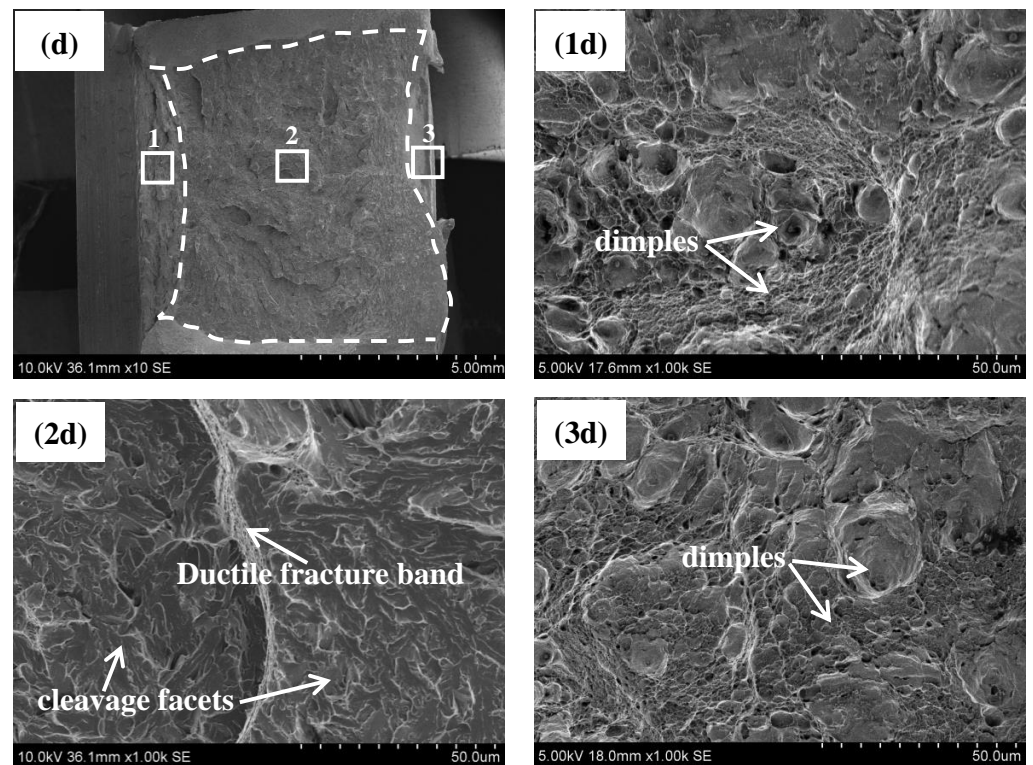


Figure 7. Macrographs showing low-magnification views (a–d) of the fracture surface in the Charpy impact specimens of (a) 0B-870, (b) 50B-870, (c) 0B-1050, and (d) 50B-1050; SEM fractographs showing high-magnification views of the crack initiation zone (1a–1d), the unstable crack propagation zone (2a–2d), and the shear-lip zone (3a–3d).

4. Discussion

According to the above results, the effects of B on the microstructures and the corresponding Charpy impact toughness of medium-carbon CrMo steels under varying T_q were different. This is obviously related to the different states of B, such as solid solution, segregation, or precipitation at different T_q [4,5,10]. Therefore, the states of B under different T_q and the effects on the microstructures and impact toughness are analyzed and discussed in detail in this section.

4.1. The Effect of B Addition on Grain Refinement under Different T_q

It is generally believed that the beneficial effect of B on the grain refinement in microalloyed steels is related to the pinning effect of the fine precipitations on GBs and the segregation of B atoms.

The SEM micrographs of the as-quenched steels with varying B content under different T_q are shown in Figure 8. It is clear that the lath martensite composed the matrix of the whole quenched structure. However, it is worth noting that, for the 50B-870 specimen, discontinuous chains of coarse particles were mainly distributed on the PAG boundaries, which were similar to those in the as-tempered specimen. It can therefore be inferred that the coarse particle identified as M_2B in the as-tempered specimen (Figure 6e) was a residue from the quenching process. Additionally, as shown in Figure 2 and Table 2, the PAG of the 50B steel was refined at a T_q of 1050 °C compared with the 0B steel, which was probably related to the fine particles precipitated during the quenching process, while, due to the limited resolution and magnification of the SEM technique, carbon extraction replicas were used for the TEM examination to further confirm our speculations. The TEM micrograph and EDS results of the as-quenched 50B-1050 specimen are presented in Figure 9. It shows many spherical-like particles of around 50 nm distributed near the dimly discernible GBs, as shown in Figure 9a. The main components of the particles were Fe and B, and the higher

carbon atomic signal mainly came from the carbon film. Therefore, it can be determined that the precipitated particles (marked by red arrows in the figure) were most likely M_2B (Fe_2B).

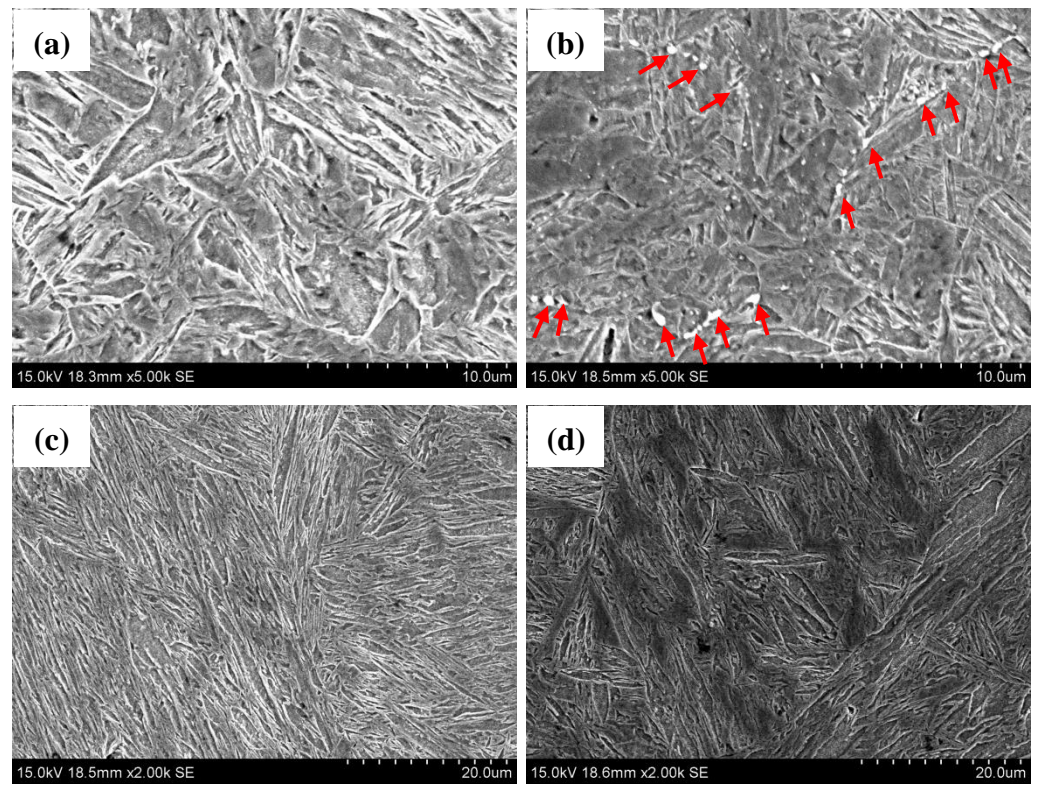


Figure 8. SEM micrographs of the quenched microstructures of (a) 0B-870, (b) 50B-870, (c) 0B-1050 and (d) 50B-1050 specimens.

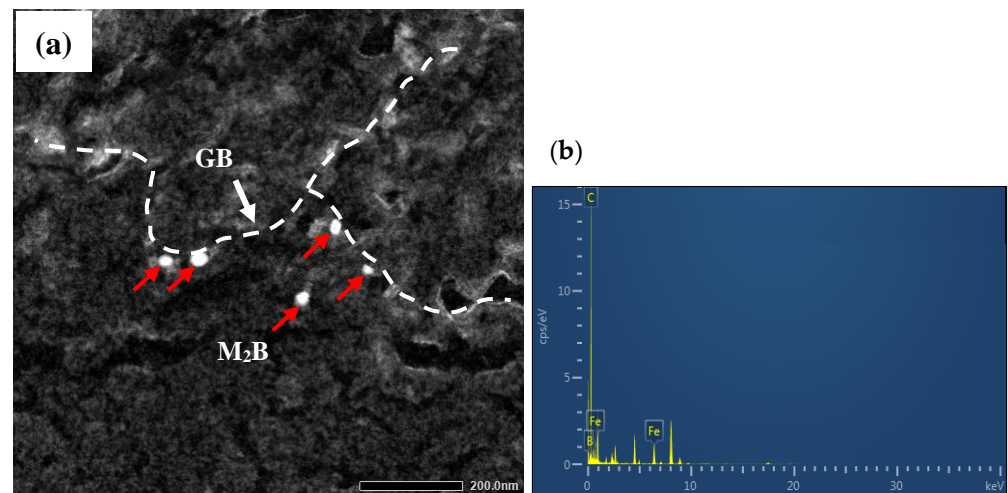


Figure 9. Typical TEM observations of the precipitates (a) and the EDS spectrum (b) of the corresponding precipitate in the as-quenched 50B-1050 specimen.

The curve of the element components and mass fraction of M_2B varying with the temperature for 50B steel was calculated and drawn by using Thermal-Calc software (Version 4.0.0.4367) and TCFE7 Database, as shown in Figure 10. It shows that the element components of M_2B are mainly Fe, Mo, Cr, and B, and the dissolved temperature of M_2B , short for T_{M_2B} , for the 50B steel was around 1073 °C, which was higher than that of the 0.27C-1.1Cr-0.5Mo-0.06V-0.04Nb-0.002B steel calculated by Zheng [4]. The difference in

the T_{M_2B} value might be due to the higher content of Mo, Cr, and B in our tested steels. In addition, since the T_q for the sample finished at 870 °C was lower than 1073 °C (T_{M_2B} of 50B steel), numerous undissolved M_2B particles remained after QT treatment and might act as crack initiation sites, seriously decreasing the toughness. On the other hand, the M_2B dissolved significantly as the T_q increased from 870 °C to 1050 °C, as shown in Figure 10, leading to a remarkable increase in the solute B concentration. As indicated by previous researchers [14], NES becomes the dominant mechanism when the quenching temperature is above 950 °C. Therefore, the solute B atoms might move to the GBs because of NES mechanisms. Furthermore, the magnitude of the NES increased with an increasing quenching temperature [14]. Thus, the segregation of B on the GBs reached the maximum and exceeded the optimum value, which promoted the new M_2B precipitation on the GBs with the T_q increasing from 870 °C to 1050 °C in this experiment. Moreover, the low driving force for precipitation growth due to the low precipitate supersaturation at a T_q of 1050 °C might explain the small sizes of the M_2B in the as-quenched 50B-1050 specimen. Finally, the possibility of crack initiation caused by undissolved M_2B decreased significantly and the toughness was improved due to the great magnitude dissolution of the M_2B and fine M_2B newly precipitated despite the existence of a small amount of undissolved M_2B and the coarsened microstructure under the high T_q of 1050 °C.

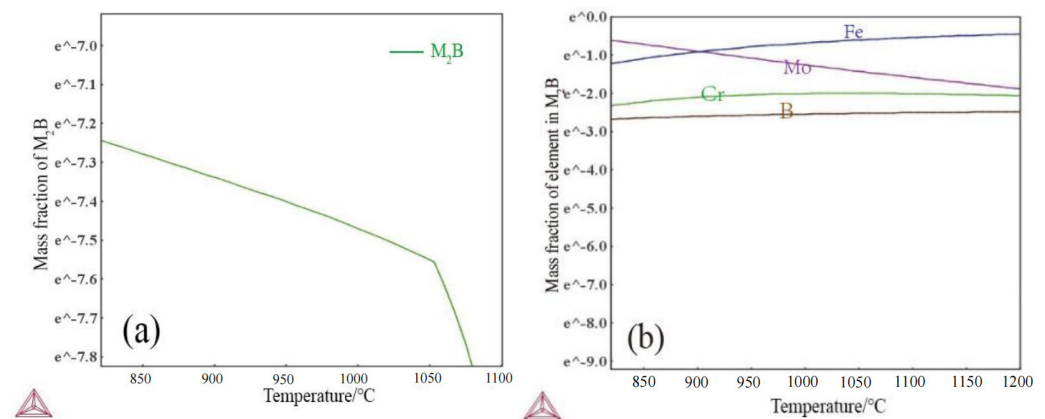


Figure 10. Thermodynamic calculation results: the precipitate of M_2B in the 50B-1050 specimen (a) and the compositions of M_2B (b).

Generally, GBs bend across second-phase particles in the growth process of the PAG. The austenite grain growth is mainly retarded by the Zener drag, and the PAG size is proportional to the average diameter of the particles and inversely proportional to the volume fraction. Therefore, the effects of B on the PAG refinement under varying T_q can be explained as follows. When quenched at 870 °C, the undissolved M_2B particles were too large to perform the pinning effect on the GBs. On the other hand, the excessive precipitation of the M_2B led to a low solute B concentration, and then, the magnitude of the B segregation on the GBs, which was beneficial for grain refinement, decreased accordingly. Therefore, no significant refinement was observed with 50 ppm B-added steel under the T_q of 870 °C. However, when the 50B steel was quenched at 1050 °C, the dissolution of the M_2B increased and a small amount of new M_2B was precipitated, which was small enough to serve as a barrier to hinder GB movement. In addition, the increased solubility of the B atoms led to an increased magnitude of B segregation, which could also reduce the GB migration in some way. Finally, the combined influence of the pinning effect of the fine precipitation of M_2B and the segregation B atoms on the GBs resulted in a significant reduction in the grain size of the austenite for the 50B-1050 specimen. As the packet and block in martensite can be simultaneously refined with PAG refinement, as demonstrated in our previous research [37], the sizes of the packet and block in the 50B-1050 specimen were smaller than those of 0B-1050. However, the grain coarsening caused by the high T_q

is unavoidable, so the grain sizes of the PAG, packet, and block of the specimen quenched at 1050 °C were all larger than those of that quenched at 870 °C.

4.2. The Effect of B Addition on Precipitates in As-Tempered Specimens under Different T_q

When 50 ppm B was added to steel, the average particle size on the GBs increased under the T_q of 870 °C but decreased under the T_q of 1050 °C.

For the 50B-870 specimen, it is obvious that the undissolved coarse M_2B due to the low T_q resulted in a larger average particle size on the GBs than that of 0B-870. Regarding the T_q of 1050 °C, B was found in refined $M_{23}C_6$ on the GBs, implying an inhibitory effect of B addition on $M_{23}C_6$ coarsening. Many studies have focused on the refinement mechanism of $M_{23}C_6$ by using B addition [19,38]. For example, Liu et al. [19] showed that interstitial B atoms would move to a growing precipitate and retard the coarsening rate of the $M_{23}C_6$ due to the low B solubility. Moreover, as reported by Hattestrand et al. [30], the coarsening rate of carbide was governed not only by diffusion coefficients but also by the equilibrium molar fractions in the matrix. The low solubility of B could be the rate-controlling element and hinder $M_{23}C_6$ from coarsening. Furthermore, since the segregation energy of B at the PAG boundaries was higher than that of C [38], it is possible that the nucleation and growth of $M_{23}C_6$ were kinetically retarded at the PAG boundaries by reducing the segregation and diffusivity of C and other carbide-forming elements. As the segregated B atoms could gradually seep into the lath, block, and packet boundaries near the PAG boundaries during tempering, the $M_{23}C_6$ on these boundaries might also be refined.

Consequently, a low B solubility and a substitutional diffusion mechanism in combination with the inhibitory effect on carbide-forming elements could explain the refined $M_{23}C_6$ in the 50B-1050 specimen.

4.3. The Relationship between B Addition, Precipitates, and Impact Toughness

It is known that large boundary carbides often have detrimental effects on impact toughness [19–21]. Due to the difference in micro-hardness between the alloying carbide and the ferrite matrix [39], a local stress concentration generates around the hard alloying carbide when the soft ferrite matrix undergoes an initial plastic deformation during the impact test. As a result, microcracks nucleate and propagate from the boundary carbides if the locally concentrated stress exceeds the critical stress, which can be described quantitatively with the classic Griffith local cracking model [40], as given in Equation (5):

$$\sigma_c = \frac{2E\gamma_s^{\frac{1}{2}}}{\alpha a} \quad (5)$$

where σ_c is the critical stress, E is the Young modulus, γ_s is the effective surface energy of the interface fracture between the hard alloying carbide and the ferrite matrix, and α is a constant related to the crack shape. Figure 11 shows the second microcracks underneath the fracture surface of the Charpy impact samples for 50B-1050. As the microcrack often nucleates at or around large carbide particles on GBs, which can be confirmed by Figure 11, a is the size of the microcrack nucleating at or around the boundary carbides.

According to the above model, the coarse boundary carbides can cause a decrease in the critical stress, resulting in the nucleation and propagation of microcracks. For the 50B-870 specimen, continuous chain-like M_2B of around 420 nm was precipitated, leading to a decreased critical stress. Then, the nucleation and propagation of microcracks occurred more easily, which was primarily responsible for the lower impact toughness. By contrast, for steels quenched at 1050 °C, a 50 ppm B content was obviously to be beneficial for the toughness at low temperatures. This can be attributed to the great difficulty with which the microcracks nucleate and propagate with respect to the smaller size of the $M_{23}C_6$ at GBs.

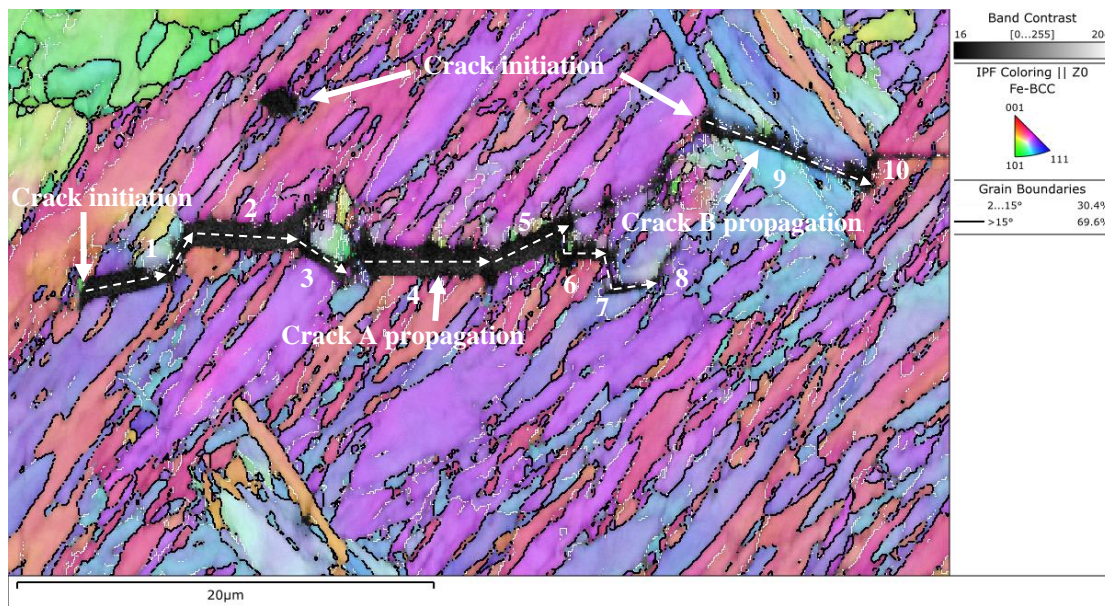


Figure 11. Typical inverse pole figure map displaying GBs with different crystal orientations in the 50B-1050 specimen. The dotted arrow line shows the crack propagation direction.

4.4. The Relationship between GBs and Impact Toughness

The variation tendency of $D_{GBMA \geq 15^\circ}$ was consistent with the size of the PAG and martensitic substructure (packet and block), suggesting some special orientation characteristics of the above GBs. Therefore, the GBMA distributions of the microstructure in the 50B-1050 sample were analyzed using EBSD and are shown in Figure 12. In particular, the martensitic block boundaries both in an identical packet and between two adjacent packets and the PAG were displayed with the EBSD orientation map and are presented in Figure 12. The corresponding GBMAs are summarized in Table 3, which shows that the GBMAs of the martensitic block boundaries in an identical packet and between two adjacent packets and the PAG were in the ranges of $55\text{--}59^\circ$, $50\text{--}56^\circ$, and $37\text{--}49^\circ$, respectively, while the GBMAs within the block containing several individual laths were less than 10° . This implies that the HAGBs were mainly due to the PAG, packet, and block, the GBMAs of which were in descending order. This is basically in agreement with Liang et al. [41,42]. Therefore, the refined grain size generated by a low T_q or B addition led to the high $D_{GBMA \geq 15^\circ}$.

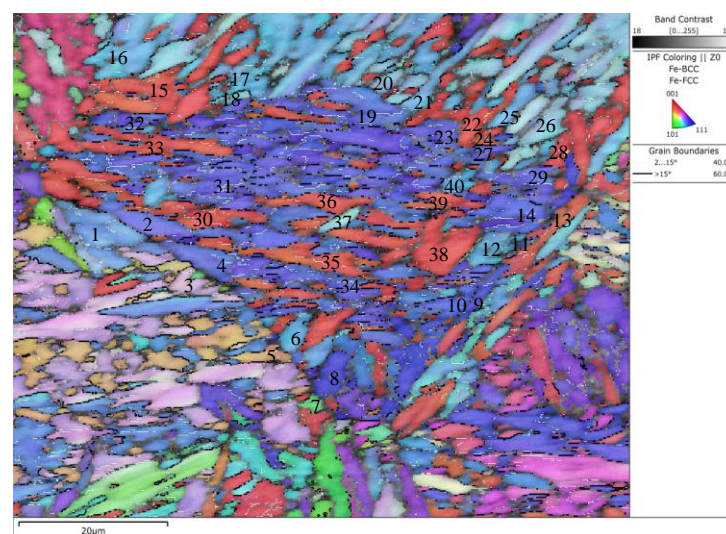


Figure 12. Typical EBSD orientation map of martensitic substructures in the 50B-1050 specimen.

Table 3. GBMAs for martensitic substructures in the 50B-1050 specimen, as illustrated in Figure 12.

Zone	Boundary of Two Blocks	GBMA/ ^o
Austenite	1–2	39.45
	3–4	42.85
	5–6	37.71
	7–8	43.83
	9–10	49.74
	11–12	46.89
	13–14	37.61
Packet	15–16	54.88
	17–18	54.71
	19–20	52.92
	19–21	55.79
	22–23	52.80
	24–25	56.31
	26–27	51.75
28–29	50.40	
Block	2–30	59.46
	30–31	57.61
	32–33	57.77
	34–35	56.03
	36–37	55.80
	38–14	56.34
39–40	51.85	

The impact toughness is associated not only with crack initiation but also with crack propagation for medium-carbon CrMo steel. As shown in previous research, the HAGB distribution undoubtedly affects the crack-propagating process and the ultimate impact toughness [40]. Hence, the crack-propagating process was studied systematically in terms of the crystallography.

Based on the speculations mentioned above, the corresponding misorientation angles between the grains adjacent to the crack in Figure 11 were analyzed with EBSD and are shown Table 4. The LAGBs/HAGBs were generally defined as GBs with misorientation angles of $2\text{--}15^\circ$ / $>15^\circ$, as indicated by the white/black line. It can be seen that microcrack A (B) propagated unimpededly through the LAGBs within the grains, e.g., 1–7 and 9, indicating that the LAGBs could not hinder the propagation of the impact crack. In contrast, microcrack A (B) changed direction when it came across the HAGBs of the grains, e.g., 1 and 2 (6 and 7), and was finally arrested at the HAGBs of grains 7 and 8 (9 and 10). Hence, the higher the $D_{\text{GBMA} \geq 15^\circ}$ of the microstructure, the more the crack deviated and the higher the impact toughness. Furthermore, the block could be the minimum structure unit controlling crack propagation.

Table 4. Effects of HAGBs on the impact crack propagation behavior shown in Figure 11.

Grain Boundary	Misorientation Angle/ ^o	Cracking Behavior
1–2	53.58	Deviated
2–3	60.64	Deviated
3–4	55.26	Deviated
4–5	53.79	Deviated
5–6	56.97	Deviated
6–7	57.65	Deviated
7–8	52.66	Arrested
9–10	44.20	Arrested

In Figure 13, the synergistic effect of B and T_q on the impact toughness after QT treatment is schematically illustrated based on the current experimental results. For the 50B-870 steel, the undissolved M_2B coarsened during the holding process due to the excess

B content combined with the low T_q and was retained in the subsequent tempering process, which resulted in a decreased critical stress and corresponding impact toughness, compared with the 0B-870 steel.

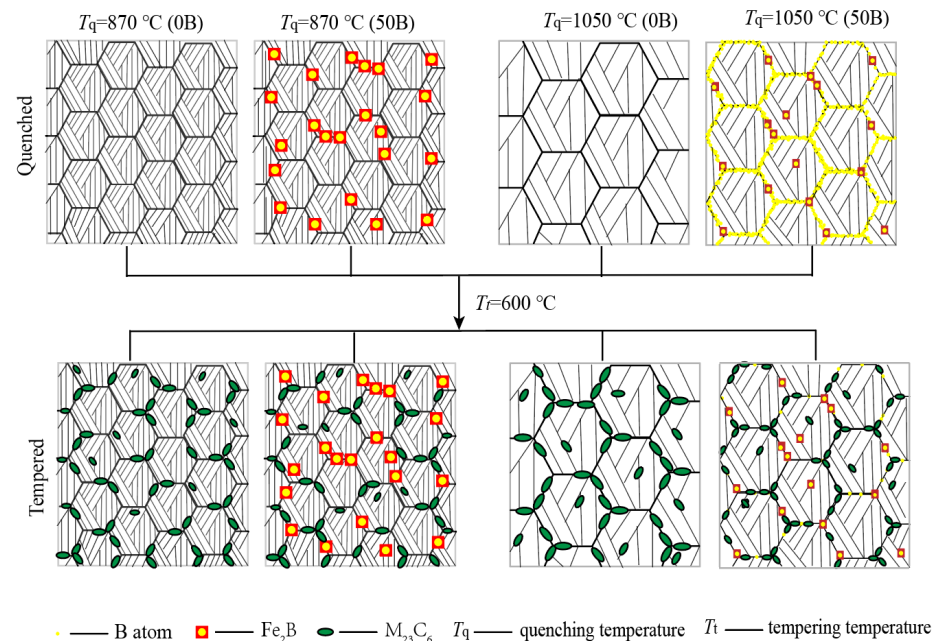


Figure 13. Schematic illustration showing the effect of the T_q on the microstructure evolution of steels with a varying B content.

However, this detrimental effect on the impact toughness could be mitigated by quenching at higher temperatures, e.g., 1050 °C in this experiment, where new finer M_2B formed due to the higher dissolving temperature and lower M_2B precipitate supersaturation. The fine M_2B particles resulted in a decreased block size and increased $D_{GBMA \geq 15^\circ}$ compared to that of 0B-1050. Moreover, B segregation on the GBs, which was primarily involved in the NES mechanism, refined the $M_{23}C_6$ during the tempering process. Both the refined $M_{23}C_6$ and the increased $D_{GBMA \geq 15^\circ}$ contributed to reducing the critical stress for crack initiation and increasing the energy required for crack propagation, finally improving the impact toughness of 50B-1050. However, the grain coarsening caused by a high T_q , which led to a lower $D_{GBMA \geq 15^\circ}$ and ultimately poor impact toughness for 50B-1050, was to some extent unavoidable. However, B can mitigate some of the detrimental effects caused by a high T_q .

In the future, more in-depth studies are required to further clarify the mechanism, focusing on the effect of B segregation on the refinement of the $M_{23}C_6$ and block.

5. Conclusions

In summary, the effects of B addition on the microstructures and impact toughness of medium-carbon CrMo steel under different T_q were investigated in this study. The following conclusions were obtained based on the systematic analysis:

(1) When the steels were quenched at a relatively low T_q , e.g., 870 °C and 950 °C, the average Charpy absorbed energy tested at -80 to -20 °C decreased significantly with an increasing B content from 0 to 50 ppm, but it increased conversely when the steels were quenched at a higher T_q of 1050 °C.

(2) For the 50B-870 steel, the undissolved M_2B coarsened during the holding process due to the excess B content combined with the low T_q and was retained in the subsequent tempering, resulting in a decreased critical stress and corresponding impact toughness, compared with the 0B-870 steel.

(3) For the 50B-1050 steel, new and finer M_2B formed due to the higher dissolving temperature and lower M_2B precipitate supersaturation, resulting in a decreased block size

and increased $D_{GBMA \geq 15^\circ}$ compared with those of 0B-1050. Moreover, the B atoms segregated on the GBs refined the $M_{23}C_6$ during the tempering process. Both the refined $M_{23}C_6$ particles on the GBs and the block contributed to reducing the critical stress for crack initiation and increasing the energy required for crack propagation, finally improving the impact toughness of the 50B-1050 steel. The poor impact toughness caused by the high T_q , which led to the grain coarsening and the accordingly lower $D_{GBMA \geq 15^\circ}$, was unavoidable to some extent. However, B addition can mitigate some detrimental effects caused by the high T_q .

Author Contributions: Conceptualization, Q.W. (Qian Wang); Software, K.L.; data curation, Q.W. (Qiang Wang), C.L.; formal analysis, Q.W. (Qiang Wang), C.L., K.L.; funding acquisition, Q.W. (Qian Wang), C.L., K.L.; investigation, Q.W. (Qiang Wang); project administration, Q.W. (Qingfeng Wang); resources, Q.W. (Qian Wang) and Q.W. (Qingfeng Wang); supervision, Q.W. (Qian Wang); validation, Q.W. (Qiang Wang); writing—original draft, Q.W. (Qiang Wang); writing—review and editing, Q.W. (Qian Wang) and Q.W. (Qingfeng Wang). All authors have read and agreed to the published version of the manuscript.

Funding: This work was supported by the Youth Fund of the Hebei Natural Science Fund Project under Grant No. E2020409029; the University Student Innovation and Entrepreneurship Training Project of Hebei under Grant No. CX-2023-024-S; the Education Department Science Research project of Hebei under Grant No. BJK2024114; the Education Department Science Research project of Hebei under Grant No. QN2022039 and the Education Department Science Research Project of Hebei under Grant No. ZD2022112.

Data Availability Statement: The raw data supporting the conclusions of this article will be made available by the authors on request.

Conflicts of Interest: The authors declare that they have no known competing financial interests or personal relationships that could have appeared to influence the work reported in this article.

References

- Pratesa, Y.; Rizkia, V.; Rahwinarni, N.; Wahyuadi Soedarsono, J. Comparison of 3%-Cr steel and carbon steel corrosion behavior as well tubing materials in CO_2 - H_2S environment. *J. Adhes. Sci. Technol.* **2022**, *37*, 2871–2884. [[CrossRef](#)]
- Li, F. Investigation on impact absorbed energy index of drill pipe. *Eng. Fail. Anal.* **2020**, *118*, 104823. [[CrossRef](#)]
- Klenam, D.E.P.; Chown, L.H.; Papo, M.J.; Cornish, L.A. Phase proportions, carbon equivalent, mechanical properties and their effect on material cost of railway axle steels. *MRS Adv.* **2018**, *3*, 2169–2181. [[CrossRef](#)]
- Zheng, Y.; Wang, F.; Li, C.; He, Y. Dissolution and precipitation behaviors of boron bearing phase and their effects on hardenability and toughness of 25CrMoNbB steel. *Mater. Sci. Eng. A* **2017**, *701*, 45–55. [[CrossRef](#)]
- Bai, J.; Jin, S.; Liang, C.; Li, X.; You, Z.; Zhao, Y.; Liu, L.; Sha, G. Microstructural origins for quench cracking of a boron steel: Boron distribution. *Mater. Charact.* **2022**, *190*, 112022. [[CrossRef](#)]
- Białobrzaska, B. The influence of boron on the resistance to abrasion of quenched low-alloy steels. *Wear* **2022**, *500–501*, 204345. [[CrossRef](#)]
- Hong, S.; Shin, S.Y.; Lee, J.; Lee, C.-H.; Lee, S. Effect of phosphorous and boron addition on microstructural evolution and Charpy impact properties of high-phosphorous-containing plain carbon steels. *Mater. Sci. Eng. A* **2013**, *564*, 461–472. [[CrossRef](#)]
- Yamaguchi, M. First-Principles Study on the Grain Boundary Embrittlement of Metals by Solute Segregation: Part I. Iron (Fe)-Solute (B, C, P, and S) Systems. *Metall. Mater. Trans. A* **2010**, *42*, 319–329. [[CrossRef](#)]
- Hashimoto, M.; Ishida, Y.; Wakayama, S.; Yamamoto, R.; Doyama, M.; Fujiwara, T. Atomistic studies of grain boundary segregation in Fe-P and Fe-B alloys—II. Electronic structure and intergranular embrittlement. *Acta Metall.* **1984**, *32*, 13–20. [[CrossRef](#)]
- Taylor, K.A. Grain-Boundary Segregation and Precipitation of Boron in 0.2 Percent Carbon Steels. *Metall. Trans. A* **1992**, *23*, 107–119. [[CrossRef](#)]
- Song, S.-H.; Faulkner, R.G.; Flewitt, P.E.J. Effect of boron on phosphorus-induced temper embrittlement. *Journal of materials science. J. Mater. Sci.* **1999**, *34*, 5549–5556. [[CrossRef](#)]
- Mun, D.J.; Shin, E.J.; Cho, K.C.; Lee, J.S.; Koo, Y.M. Cooling Rate Dependence of Boron Distribution in Low Carbon Steel. *Metall. Mater. Trans. A* **2011**, *43*, 1639–1648. [[CrossRef](#)]
- Gárlipp, W.; Cilense, M.; Gomes, S.I.N. Austenite decomposition of C-Mn steel containing boron by continuous cooling. *J. Mater. Process. Technol.* **2001**, *114*, 71–74. [[CrossRef](#)]
- Da Rosa, G.; Maugis, P.; Portavoce, A.; Drillet, J.; Valle, N.; Lentzen, E.; Hoummada, K. Grain-boundary segregation of boron in high-strength steel studied by nano-SIMS and atom probe tomography. *Acta Mater.* **2020**, *182*, 226–234. [[CrossRef](#)]
- Aust, K.T.; Hanneman, R.E.; Niessen, P.; Westbrook, J.H. Solute induced hardening near grain boundaries in zone refined metals. *Acta Metall.* **1968**, *16*, 291–302. [[CrossRef](#)]
- Hwang, B.; Suh, D.-W.; Kim, S.-J. Austenitizing temperature and hardenability of low-carbon boron steels. *Scr. Mater.* **2011**, *64*, 1118–1120. [[CrossRef](#)]

17. Cao, R.; Han, C.; Guo, X.; Jiang, Y.; Liao, F.; Yang, F.; Dou, G.; Yan, Y.; Chen, J. Effects of boron on the microstructure and impact toughness of weathering steel weld metals and existing form of boron. *Mater. Sci. Eng. A* **2022**, *833*, 142560. [[CrossRef](#)]
18. Mishnev, R.; Dudova, N.; Dudko, V.; Kaibyshev, R. Impact toughness of a 10% Cr steel with high boron and low nitrogen contents. *Mater. Sci. Eng. A* **2018**, *730*, 1–9. [[CrossRef](#)]
19. Liu, F.; Fors, D.H.R.; Golpayegani, A.; Andrén, H.-O.; Wahnström, G. Effect of Boron on Carbide Coarsening at 873 K (600 °C) in 9 to 12 pct Chromium Steels. *Metall. Mater. Trans. A* **2012**, *43*, 4053–4062. [[CrossRef](#)]
20. Hättestrand, M.; Andrén, H.-O. Boron distribution in 9–12% chromium steels. *Mater. Sci. Eng. A* **1999**, *270*, 33–37. [[CrossRef](#)]
21. Osanai, T.; Sekido, N.; Yonemura, M.; Maruyama, K.; Takeuchi, M.; Yoshimi, K. Evolution of boron segregation during tempering in B doped 9%Cr ferritic steel. *Mater. Charact.* **2021**, *177*, 111192. [[CrossRef](#)]
22. Paravicini Bagliani, E.; Santofimia, M.J.; Zhao, L.; Sietsma, J.; Anelli, E. Microstructure, tensile and toughness properties after quenching and partitioning treatments of a medium-carbon steel. *Mater. Sci. Eng. A* **2013**, *559*, 486–495. [[CrossRef](#)]
23. Zhou, T.; Yu, H.; Wang, S. Effect of microstructural types on toughness and microstructural optimization of ultra-heavy steel plate: EBSD analysis and microscopic fracture mechanism. *Mater. Sci. Eng. A* **2016**, *658*, 150–158. [[CrossRef](#)]
24. Zhang, C.-y.; Wang, Q.-f.; Kong, J.-l.; Xie, G.-z.; Wang, M.-z.; Zhang, F.-c. Effect of Martensite Morphology on Impact Toughness of Ultra-High Strength 25CrMo48V Steel Seamless Tube Quenched at Different Temperatures. *J. Iron Steel Res. Int.* **2013**, *20*, 62–67. [[CrossRef](#)]
25. Yang, Z.; Liu, Z.; He, X.; Qiao, S.; Xie, C. Effect of microstructure on the impact toughness and temper embrittlement of SA508Gr.4N steel for advanced pressure vessel materials. *Sci. Rep.* **2018**, *8*, 207. [[CrossRef](#)] [[PubMed](#)]
26. Kang, J.; Wang, C.; Wang, G.D. Microstructural characteristics and impact fracture behavior of a high-strength low-alloy steel treated by intercritical heat treatment. *Mater. Sci. Eng. A* **2012**, *553*, 96–104. [[CrossRef](#)]
27. Alhassan, M.; Bashiru, Y. Carbon Equivalent Fundamentals in Evaluating the Weldability of Microalloy and Low Alloy Steels. *World J. Eng. Technol.* **2021**, *09*, 782–792. [[CrossRef](#)]
28. ASTM E23-18a; Standard Test Methods for Notched Bar Impact Testing of Metallic Materials. ASTM-International: West Conshohocken, PA, USA, 2018.
29. Stormvinter, A.; Miyamoto, G.; Furuhashi, T.; Hedström, P.; Borgenstam, A. Effect of carbon content on variant pairing of martensite in Fe–C alloys. *Acta Mater.* **2012**, *60*, 7265–7274. [[CrossRef](#)]
30. Terasaki, H.; Komizo, Y.-i. Morphology and Crystallography of Bainite Transformation in a Single Prior-Austenite Grain of Low-Carbon Steel. *Metall. Mater. Trans. A* **2013**, *44*, 2683–2689. [[CrossRef](#)]
31. Clarke, A.J.; Miller, M.K.; Field, R.D.; Coughlin, D.R.; Gibbs, P.J.; Clarke, K.D.; Alexander, D.J.; Powers, K.A.; Papin, P.A.; Krauss, G. Atomic and nanoscale chemical and structural changes in quenched and tempered 4340 steel. *Acta Mater.* **2014**, *77*, 17–27. [[CrossRef](#)]
32. Wang, Y.; Sun, J.; Jiang, T.; Sun, Y.; Guo, S.; Liu, Y. A low-alloy high-carbon martensite steel with 2.6 GPa tensile strength and good ductility. *Acta Mater.* **2018**, *158*, 247–256. [[CrossRef](#)]
33. Liu, W.; Wang, X.; Guo, F.; Shang, C. Carbides Dissolution in 5Cr15MoV Martensitic Stainless Steel and New Insights into Its Effect on Microstructure and Hardness. *Materials* **2022**, *15*, 8742. [[CrossRef](#)] [[PubMed](#)]
34. Gururaj, K.; Pal, S. Influence of dislocation density and grain size on precipitation kinetics on P92 grade steel. *Mater. Today Proc.* **2019**, *18*, 1364–1374. [[CrossRef](#)]
35. Saha, D.C.; Biro, E.; Gerlich, A.P.; Zhou, Y. Martensite tempering kinetics: Effects of dislocation density and heating rates. *Mater. Charact.* **2020**, *168*, 110564. [[CrossRef](#)]
36. Bouyne, E.; Flower, H.M.; Lindley, T.C.; Pineau, A. Use of EBSD technique to examine microstructure and cracking in a bainitic steel. *Scr. Mater.* **1998**, *39*, 295–300. [[CrossRef](#)]
37. Wang, Q.; Sun, Y.; Shi, G.; Meng, K.; Wang, Q.; Zhang, F. Effect of niobium on sulfide stress cracking behavior of tempered martensitic steel. *Corros. Sci.* **2020**, *165*, 108387. [[CrossRef](#)]
38. Karlsson, L.; Nordén, H. Overview no. 63 Non-equilibrium grain boundary segregation of boron in austenitic stainless steel-II. Fine scale segregation behaviour. *Acta Metall.* **1988**, *36*, 13–24. [[CrossRef](#)]
39. Li, X.; Ma, X.; Subramanian, S.V.; Shang, C.; Misra, R.D.K. Influence of prior austenite grain size on martensite–austenite constituent and toughness in the heat affected zone of 700 MPa high strength linepipe steel. *Mater. Sci. Eng. A* **2014**, *616*, 141–147. [[CrossRef](#)]
40. Zhang, Y.; Shi, G.; Sun, R.; Guo, K.; Zhang, C.; Wang, Q. Effect of Si content on the microstructures and the impact properties in the coarse-grained heat-affected zone (CGHAZ) of typical weathering steel. *Mater. Sci. Eng. A* **2019**, *762*, 138082. [[CrossRef](#)]
41. Liang, Y.; Long, S.; Xu, P.; Lu, Y.; Jiang, Y.; Liang, Y.; Yang, M. The important role of martensite laths to fracture toughness for the ductile fracture controlled by the strain in EA4T axle steel. *Mater. Sci. Eng. A* **2017**, *695*, 154–164. [[CrossRef](#)]
42. Li, S.; Zhu, G.; Kang, Y. Effect of substructure on mechanical properties and fracture behavior of lath martensite in 0.1C–1.1Si–1.7Mn steel. *J. Alloys Compd.* **2016**, *675*, 104–115. [[CrossRef](#)]

Disclaimer/Publisher’s Note: The statements, opinions and data contained in all publications are solely those of the individual author(s) and contributor(s) and not of MDPI and/or the editor(s). MDPI and/or the editor(s) disclaim responsibility for any injury to people or property resulting from any ideas, methods, instructions or products referred to in the content.